World Scientific
www.worldscientific.com

High-resolution polarization-sensitive optical coherence tomography and optical coherence tomography angiography for zebrafish skin imaging

Di Yang, Zhuoqun Yuan, Zihan Yang, Muyun Hu and Yanmei Liang*

Institute of Modern Optics, Nankai University
Tianjin Key Laboratory of Micro-scale Optical Information Science
and Technology, Tianjin 300350, P. R. China
*ymliang@nankai.edu.cn

Zebrafish is an important animal model, which is used to study development, pathology, and genetic research. The zebrafish skin model is widely used in cutaneous research, and angiogenesis is critical for cutaneous wound healing. However, limited by the penetration depth, the available optical methods are difficult to describe the internal skin structure and the connection of blood vessels between the skin and subcutaneous tissue. By a homemade high-resolution polarization-sensitive optical coherence tomography (PS-OCT) system, we imaged the polarization contrast of zebrafish skin and the zebrafish skin vasculature with optical coherence tomography angiography (OCTA). Based on these OCT images, the spatial distribution of the zebrafish skin vasculature was described. Furthermore, we monitored the healing process of zebrafish cutaneous wounds. We think the high-resolution PS-OCT system will be a promising tool in studying cutaneous models of zebrafish.

Keywords: Polarization-sensitive optical coherence tomography; optical coherence tomography angiography; zebrafish; skin vasculature.

1. Introduction

Cutaneous wound healing is a complex multi-step process including hemostasis, inflammation, proliferation, and maturation.[1,2] In the proliferation stage, endothelial cells form a microvascular network through angiogenesis.[3] In the subsequent maturation stage, new skin tissue is established through the degeneration of excessive capillaries. Thus, angiogenesis is an essential part of the cutaneous wound healing process. It has been demonstrated that adult zebrafish and adult mammals have consistent major steps and principles of cutaneous wound healing.[4] Therefore, the zebrafish has become a valuable model for studying cutaneous wound healing.[5]

Imaging of zebrafish skin is mainly based on fluorescence microscopy, coupled with imaging of methylene blue staining.[6,7] The imaging of

*Corresponding author.

methylene blue staining is used to assess the recovery degree of cutaneous wound healing, and fluorescence microscopy provides high-resolution imaging analysis. However, specific fluorescent labels are needed for different tissues of zebrafish skin, and complex pretreatments are often required before imaging.[8,9] Moreover, the skin of adult zebrafish is not transparent due to the pigmentation,[10] which decreases the penetration depth of the fluorescence microscopy. The imaging ranging from the bottom of the skin to subcutaneous tissue often relies on *ex vivo* tissue slices.

Optical coherence tomography angiography (OCTA) is an extension of optical coherence tomography (OCT) that facilitates the *in vivo* visualization of the vasculature.[11–14] OCTA can provide depth-resolved microvascular information with high spatial resolution. There have been many OCTA imaging methods[14] used to image vessels, including phase-signal-based OCTA,[15] intensity-signal-based OCTA,[16] and complex-signal-based OCTA methods.[17] Polarization-sensitive OCT (PS-OCT), as a functional extension of OCT, not only has the advantages of OCT but also indicates the polarimetric properties of samples. There have been several polarization-sensitive optical coherence tomography angiography methods to image the skin and its blood vessels.[18–21] Combining polarization contrast (from PS-OCT) and flow contrast (from OCTA), more internal skin structures can be observed than only using a standard OCT system.[21] Several zebrafish studies have used the OCT system

to image skeletal[22] and brain diseases.[23] There also have been some vascular studies in ophthalmology[24] and embryos[25] of zebrafish based on the OCTA. In our previous study, we used a PS-OCT system to image zebrafish muscle and analyzed its polarization characteristics.[26] Although the study of the skin of adult zebrafish is used as a reference for studying adult mammals' skin,[4] there is no relevant OCTA or PS-OCT imaging research on it.

In this study, the skin of zebrafish was imaged with our homemade PS-OCT system and the OCTA image of zebrafish skin vasculature was calculated. The polarization and flow characteristics of zebrafish skins at different ages (2 months and 9 months old) were investigated. Further, the spatial distribution of the vasculature from the skin to the subcutaneous tissue was analyzed with OCTA information. Finally, we monitored the healing process of zebrafish cutaneous wounds and proved the applicability of PS-OCT and OCTA in the long-term monitoring of zebrafish skin vasculatures.

2. Method

2.1. *Imaging system*

The details of our spectral domain PS-OCT system have been described previously,[26] and only a brief description is provided here. As shown in Fig. 1(a), the Michelson interferometer is illuminated with a broadband light source (BLM2-D, Superlum)
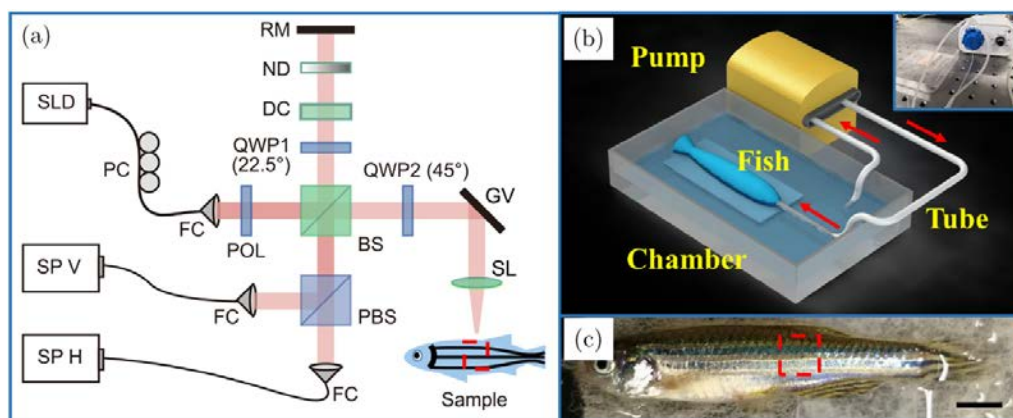

Fig. 1. (a) Experimental schematic of the PS-OCT system. Polarization optics are drawn in blue. SLD, superluminescent diode; PC, polarization controller; FC, fiber collimator; POL, linear polarizer; BS, nonpolarizing beam splitter; QWP, quarter-wave plate; DC, dispersion compensator; ND, neutral density filter; RM, reference mirror; GV, galvanometer scanning mirror; SL, scanning lens; PBS, polarizing beam splitter; SP, spectrometer; H and V, horizontal and vertical polarization state channels, respectively. (b) Experimental schematic of the anesthesia system. A picture of the anesthesia system is placed in the upper right corner of the image. (c) Zebrafish anesthesia image. The imaging area is marked by a red dashed box. The scale bar in (c) is 2.5 mm.

centered at 840 nm and a bandwidth of 100 nm. The incident light from the light source is linearly polarized and split into sample and reference arms. In the sample arm, a quarter-wave plate (QWP, at 45°) provides circularly polarized light for sample illumination. A scanning lens (LSM03-BB, Thorlabs) is used to scan the sample. The interfered light from the sample arm and the reference arm is split into two orthogonal components at the polarizing beam splitter and acquired by two commercial spectrometers (Cobra-S 800, Wasatch Photonics). Our setup provides an axial resolution of $\sim 3.4\,\mu\mathrm{m}$ in air. Compared with our previous system,[26] we optimized the transverse resolution to $\sim 8\,\mu\mathrm{m}$ in the focal plane.

For this study, each spectrometer is operated at an 80 kHz line rate. In the fast transverse scan direction, each B-scan consists of 500 A-scans over 2.5 mm. In the slow transverse scan direction, there are 500 discrete sampling planes over 2.5 mm. For improving the signal-to-noise ratio (SNR) of OCTA, eight consecutive B-scans are acquired at each slow-scan position to suppress the noise caused by convulsions and breathing fluctuation.[27]

2.2. *Data processing*

The scattering pattern of blood flow varies rapidly over time resulting in decorrelation of the received backscattered signals at different times. To improve the SNR without increasing the scan acquisition time, split-spectrum amplitude-decorrelation angiography (SSADA)[28] was used to calculate the decorrelations of blood flow and static tissues in our study.

First, the spectrum from the spectrometers is used as the interferogram after background removal and resampling to k-space. The full bandwidth of the interferogram is split via Gaussian filters into M spectral splits. The center positions of these filters are evenly spaced across the regions of the interferogram. Then, M individual interferograms are transformed into z-space using the fast Fourier transform as their intensity, I. Then, the OCTA parameter is generated from decorrelation $\overline{D}$, which can be described by

$$\overline{D} = 1 - \frac{1}{N-1}\frac{1}{M}\sum_{n=1}^{N-1}\sum_{m=1}^{M}\frac{I_{m,n}I_{m,n+1}}{\left[\frac{1}{2}I_{m,n}^2 + \frac{1}{2}I_{m,n+1}^2\right]},$$

(1)

where N is the number of B-scans taken at the same position and M is the number of spectral splits.

For our PS-OCT system, two orthogonal signal intensities, I_H and I_V (H: Horizontal, V: Vertical), are acquired by two spectrometers. For combining two orthogonal signal channels, three different calculation methods of decorrelation values are considered as OCTA parameters (Parameters 1–3) to be compared. The decorrelation values of H and V channels ($\overline{D}_H$ and $\overline{D}_V$) are calculated with $I = I_H$ and $I = I_V$, respectively. Then, we define L1-norm ($\overline{D}_1$) and L2-norm ($\overline{D}_2$) of them as OCTA Parameters 1 and 2, respectively,

$$\begin{aligned}\overline{D}_1 &= \left|\overline{D}_H\right| + \left|\overline{D}_V\right| \\ \overline{D}_2 &= \sqrt{\overline{D}_H^2 + \overline{D}_V^2}\end{aligned}.$$

(2)

Besides, the intensity of the OCT structural signal I is calculated as follows:

$$I = I_H + I_V.$$

(3)

Then, the decorrelation of the intensity ($\overline{D}_3$) can be calculated by Eq. (1) as OCTA Parameter 3.

2.3. *Sample preparation*

For phantom imaging, a polyethylene tube within a 0.05% intralipid solution was used as our flow phantom, and a peristaltic pump was used to generate a certain flow velocity. For zebrafish imaging, wild-type zebrafish of strain AB at different ages (about 2 months old and 9 months old) were used. First, zebrafish were pre-anesthetized with 0.016% tricaine solution until their gills stopped moving. Then, for the cutaneous wound experiment, we removed 2–4 scales and introduced wounds onto the flank of the zebrafish.

During the imaging, zebrafish were anesthetized with our home-built anesthesia system as shown in Fig. 1(a). A picture of the anesthesia system is placed in the upper right corner of the image. A zebrafish was mounted on a piece of cotton in a fish chamber (plastic case). The cotton acted as a support and adhesion for the zebrafish. The chamber was connected to a peristaltic pump, which allowed for 0.016% tricaine solution in a circulatory manner. The tail and mouth regions of zebrafish were covered with the solution except for the imaging area (marked by a red dashed box), as shown in Fig. 1(b). The zebrafish was intubated with a polyethylene tube, and the flow rate was set to

$\sim 4\,\mathrm{mL/min}$ by the peristaltic pump. After imaging, the zebrafish was perfused with fresh water for recovery from anesthesia. All experimental protocols using animals were approved by the Institutional Animal Care Committee of Nankai University.

3. Experimental Results

3.1. *Phantom imaging*

To select the best OCTA parameter for high contrast OCTA images, we first imaged a fluid phantom with our PS-OCT system. The decorrelation signal-to-noise ratio (DSNR)[28] is used to evaluate OCTA imaging quality. The DSNR of the flow

phantom is defined as follows:

$$\mathrm{DSNR} = \frac{\bar{D}_{\mathrm{Flow}} - \bar{D}_{\mathrm{Solid}}}{\sqrt{\sigma^2_{\mathrm{Solid}}}}, \qquad (4)$$

where $\bar{D}_{\mathrm{Flow}}$ and $\bar{D}_{\mathrm{Solid}}$ are the average decorrelation values within the flow and the solid regions, respectively, and $\sigma^2_{\mathrm{Solid}}$ is the variance of the decorrelation within the solid region.

In B-scan OCT intensity and B-scan OCTA images [Figs. 2(a) and 2(b)], the flow region (intralipid flow) and the solid region (polyethylene tube) are marked by red and yellow rectangular boxes, respectively. By adjusting the number of split-spectrums and the bandwidth of each split-spectrum, we generated a set of decorrelation
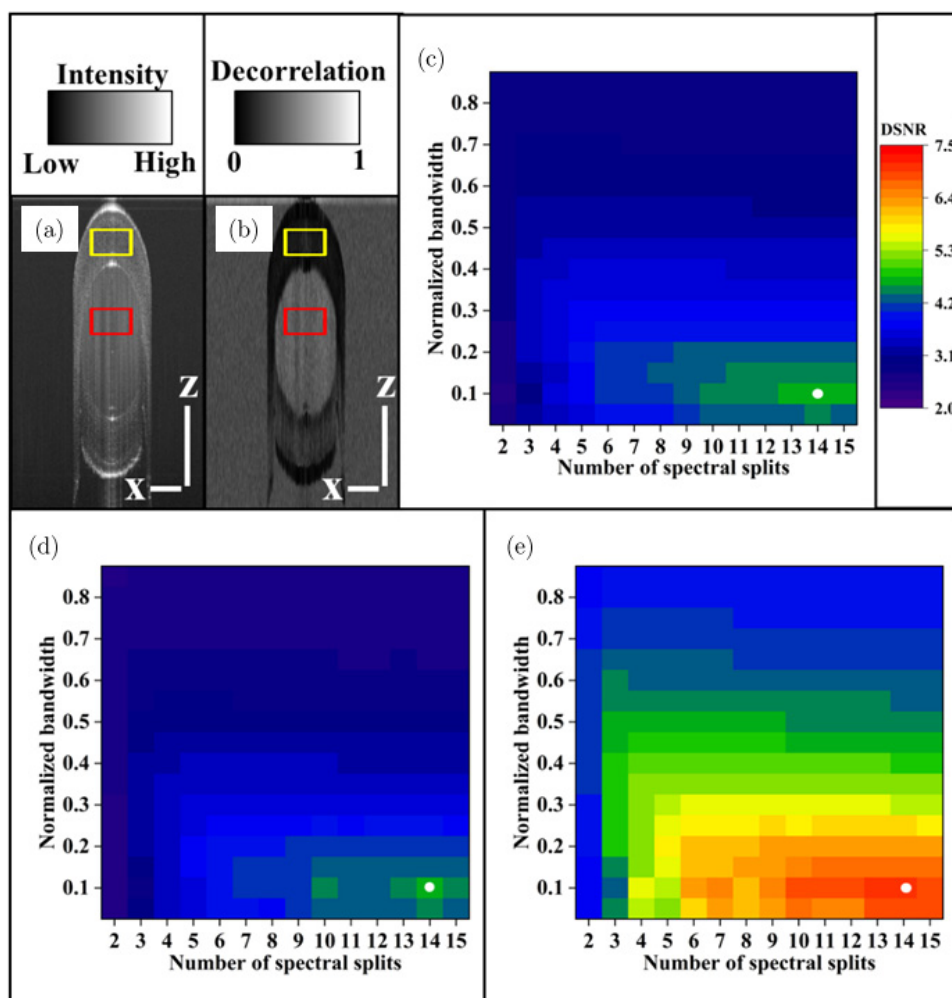

Fig. 2. The fluid phantom imaging. (a) is the B-scan OCT intensity image. (b) is the B-scan OCTA decorrelation image. The flow region (intralipid flow) and the solid region (polyethylene tube) are marked by red and yellow rectangular boxes, respectively. (c)–(e) show the relationships among the number of split-spectrums, normalized bandwidth to the system spectral bandwidth, and DSNR by using Parameters 1–3, respectively. The normalized bandwidth is defined as the ratio of the bandwidth of the Gaussian filter to the half-maximum bandwidth of the light source. Scale bars in (a) and (b) are $400\,\mu$m.

images with three parameters. The DSNR was calculated for each decorrelation image. Figures 2(c)–2(e) show the relationships among the number of split-spectrums, normalized bandwidth to the system spectral bandwidth, and DSNR by using Parameters 1–3, respectively. The normalized bandwidth is defined as the ratio of the bandwidth of the Gaussian filter to the half-maximum bandwidth of the light source. Similar to the result in Ref. 28, there is a maximum DSNR with each method at the same normalized bandwidth value of 0.1 and spectral splits number of 14, marked by white dots in Figs. 2(c)–2(e). As shown in Fig. 2(e), the maximum DSNR value of Parameter 3 is 7.08, which is larger than those of Parameters 1 and 2. Therefore, the derived parameters of 14 spectral splits and the normalized bandwidth of 0.1 were selected to calculate the OCTA image by using Parameter 3 in our study.

3.2. *Skin images of zebrafish at different ages*

Although the main steps and process of adult zebrafish cutaneous wound healing are similar to adult mammals,[4] the structure of zebrafish skin is different from that of adult mammals. The zebrafish skin system includes not only the epidermis and dermis that mammals have but also bone tissues such as the scale. The B-scan intensity image of zebrafish skin is shown in Fig. 3(a). The zebrafish scale serves as a part of the skin carrier which is a thin membranous bone embedded in the skin.[8] The transparent bone matrix of the zebrafish scale shows low intensity, as circled by orange dashed curves in Fig. 3(a). In Fig. 3(a), the small vertical lines inside each bone matrix are radial grooves marked by red arrows.

When performing *en-face* imaging on the skin, a base plane is needed for defining the depth position of the tissue, and the skin surface is generally used as the base plane.[29] However, due to the complexity of zebrafish skin structure, using the skin surface as the base plane is hard to give a detailed description in *en-face* images. In contrast, it is more reasonable to use the basal layer of zebrafish skin as the base plane, which is the basis for its skin growth. In Fig. 3(a), the basal layer as the base plane (marked by a yellow dashed curve) shows higher intensity than other layers due to its pigmentation. The area
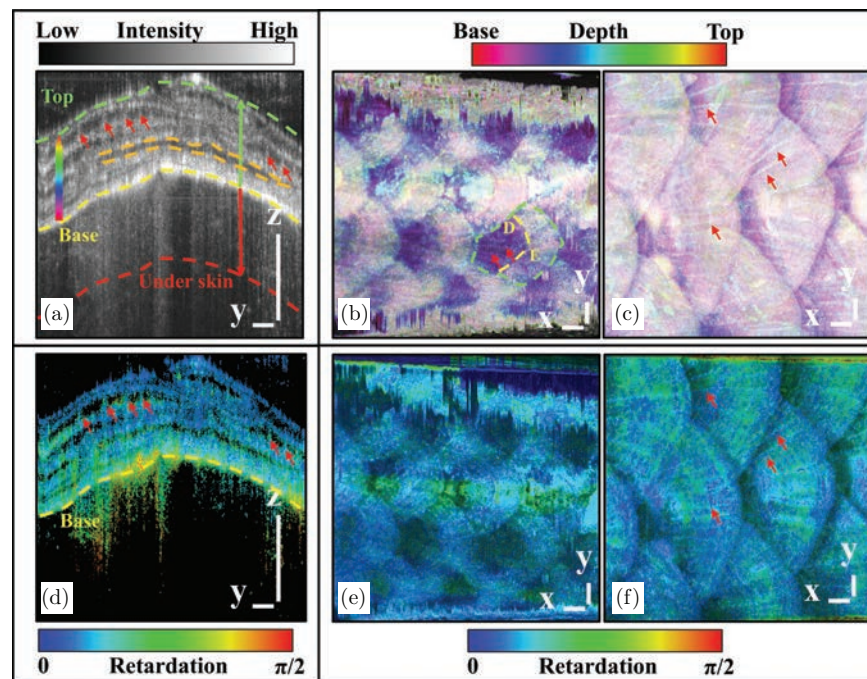

Fig. 3.   The intensity and accumulative retardation images of zebrafish skin area at different ages. (a) is the B-scan OCT intensity image of 9-month-old zebrafish skin. (b) and (c) are the depth-color encoded OCT intensity images of zebrafish at 2 and 9 months old, respectively. D and E represent the dermis and epidermis, respectively. (d) is the B-scan OCT accumulative retardation image of (a). (e) and (f) are the AIPs of accumulative retardation of the 2-month old zebrafish and the 9-month old zebrafish. All scale bars are 200 μm.

ranging from the base plane to the top of the scale (marked by a green dashed curve) is defined as the skin area. As shown in Fig. 3(a), our OCT system with enough penetration depth can achieve full depth imaging of the zebrafish skin. Furthermore, due to the high imaging depth of OCT, it can still study the connection between skin blood vessels and subcutaneous tissue blood vessels. We observed that the detection depth of the subcutaneous blood vessels exceeds 200 μm. Therefore, the area ranging from the base plane to the depth of 200 μm is selected as the subcutaneous tissue imaging area.

Based on the above definitions, we analyzed the skin structure and vasculature of the 2-month-old zebrafish and the 9-month-old zebrafish. For skin structure imaging, we calculated the depth-color encoded OCT intensity image. The depth-color encoded OCT intensity image is the *en-face* image with depth-resolved color mapping. First, *en-face* intensity images at different depths were given pseudo color according to the color bar at the top of Figs. 3(b) and 3(c). Then, we merged those pseudo color images to generate the depth-color encoded OCT intensity images, whose color indicates the depth information. The depth-color encoded OCT intensity images of zebrafish at different ages are shown in Figs. 3(b) and 3(c), respectively. In Fig. 3(b), each scale of 2-month-old zebrafish (marked by a green dashed closed curve) can be divided into two parts with high and low intensities, which are related to the epidermis part and the dermis part, respectively. The outer end of the scale matrix is wrapped by the epidermis, showing a higher intensity than the part inserted into the dermis. Moreover, we can observe several radial grooves (marked by red arrows) at the dermis part. In Fig. 3(c), the scales of 9-month-old zebrafish are larger than those of 2-month-old zebrafish. The radial grooves in the epidermal area are marked by red arrows.

In the accumulative retardation image [Fig. 3(d)], the retardation of most of the skin area is low and homogeneous. The radial grooves (marked by red arrows) and basal layer of zebrafish skin (marked by a yellow dashed curve) show high retardation because the radial grooves and the basal layer are bone and collagenous tissues, respectively, which have higher birefringence. The average intensity projection (AIPs)[30] of accumulative retardation of the 2-month-old zebrafish and the 9-month-old zebrafish is shown in Figs. 3(e) and 3(f) with a transparency of 0.5. We

observe that most of the skin area shows low retardation. The radial grooves with high retardation are marked by red arrows in Fig. 3(f).

The zebrafish, due to its stereotypic pattern of colorful stripes, has become an important model of color pattern formation in vertebrates.[31] The stripes, as shown in a photo of 9-month-old zebrafish skin [Fig. 4(a)], are observed as a multi-layered arrangement in the hypodermis.[31] The layers with silvery or blue iridophores and black melanophores are marked by two blue dashed curves. The layer with yellow xanthophores is marked by two black dashed curves. For analyzing the subcutaneous tissue, the depth-color encoded OCT intensity images of zebrafish subcutaneous areas at different ages are shown in Figs. 4(b) and 4(c), respectively. We can observe many black melanophores points in layers marked by two blue dashed curves. Black melanophores in 9-month-old zebrafish are denser than that of 2-month-old zebrafish. For accumulative retardation imaging, a B-scan accumulative retardation image is shown in Fig. 4(d). The layer with yellow xanthophores disrupts the retardation of the tissue below it (marked by black dashed lines), which may be caused by the depolarization of yellow xanthophores. More detailed descriptions can be observed in AIPs of accumulative retardation of the 2-month-old zebrafish and the 9-month-old zebrafish [Figs. 4(e) and 4(f)]. The layer with yellow xanthophores is pointed out by a high-value boundary marked by two black dashed curves. The high-value boundary is caused by the disorder of retardation, which indicates its high depolarization. Several myoseptum pointed out by blue arrows split myotome with high retardation.[26] The above result shows that the intensity and polarization images have different sensitivities to different pigments. The intensity image is sensitive to black melanophores, while the polarization image is sensitive to yellow xanthophores.

AIPs of OCTA are used to compare the blood vessel distribution of zebrafish at different ages in our study. The AIPs of OCTA within the skin area and the subcutaneous tissue area are shown in Fig. 5. Figures 5(a)–5(c) and 5(d)–5(f) are corresponding to 2-month-old and 9-month-old zebrafish, respectively. Figures 5(a) and 5(d) are AIPs of the skin area. The blood vessel of 2-month-old zebrafish composes a clear rhombus vasculature, and the nodes of the vasculature (shown by a red dashed circle) corresponds to the scale area. In
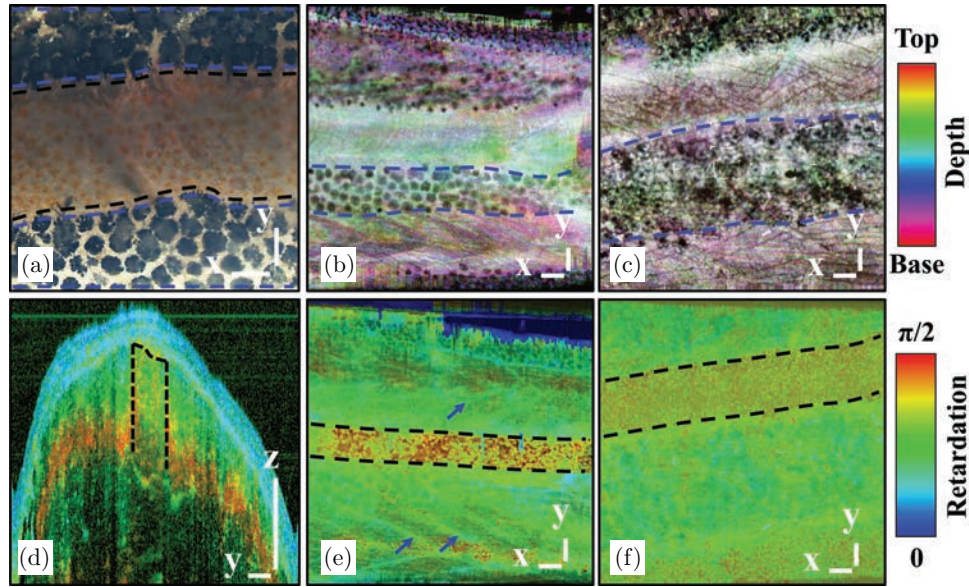
Fig. 4.   The intensity and accumulative retardation images of zebrafish subcutaneous area at different ages. (a) is the photo of a 9-month old zebrafish skin. (b) and (c) are the depth-color encoded OCT intensity images of zebrafish at 2 and 9 months old, respectively. (d) is the B-scan OCT accumulative retardation image of 2-month old zebrafish. (e) and (f) are the AIPs of accumulative retardation of the 2-month old zebrafish and the 9-month old zebrafish. All scale bars are 200 μm.
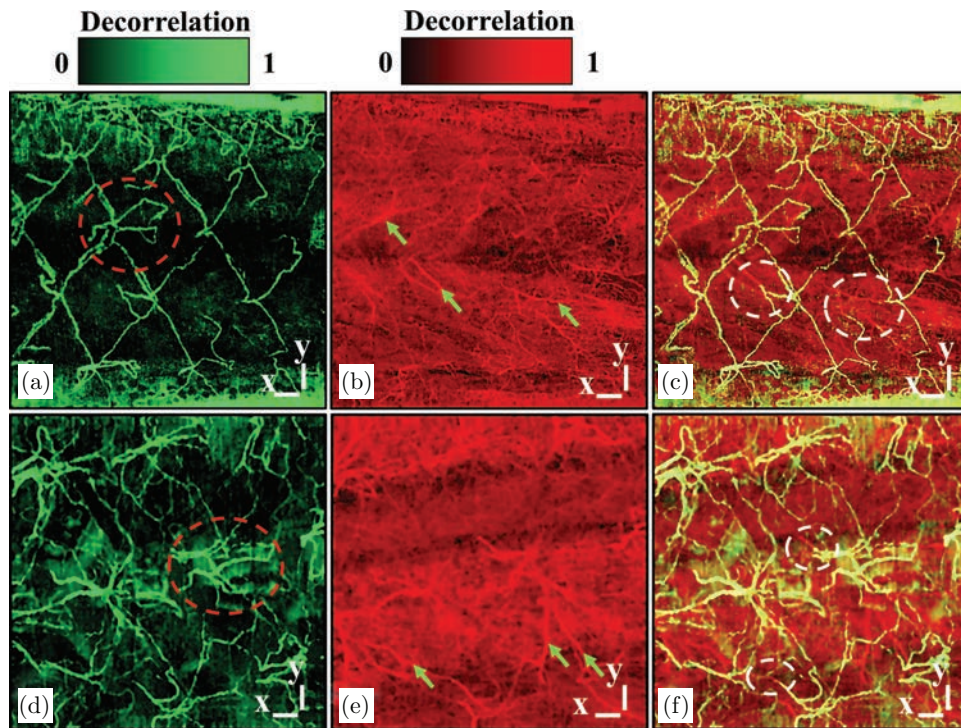

Fig. 5.   OCTA images of zebrafish at different ages. (a)–(c) and (d)–(f) are AIPs of OCTA corresponding to 2-month old zebrafish and 9-month old zebrafish, respectively. (a) and (d) are AIPs of OCTA within the skin area. (b) and (e) are AIPs of the subcutaneous tissue area. (c) and (f) are the images merging the AIPs of OCTA within the skin area and the subcutaneous tissue area. All scale bars are 200 μm.

contrast, the vasculature of 9-month-old zebrafish is more complicated, and the nodes (shown by a red dashed circle) present more diverse forms. For the subcutaneous tissue area, the distribution of blood vessels is different from that of the skin area, as shown in Figs. 5(b) and 5(e). The blood vessels are more densely distributed, and some thicker blood vessels (pointed by green arrows) are distributed in the microvascular cluster. By merging the AIPs of the skin area and the subcutaneous tissue area, we obtained Figs. 5(c) and 5(f). The blood vessels of

the skin area and the subcutaneous area are connected in some areas (marked by white dashed circles), showing the relationship between the internal and the external distribution of blood vessels in the zebrafish skin.

3.3. *Spatial distribution of the skin vasculature*

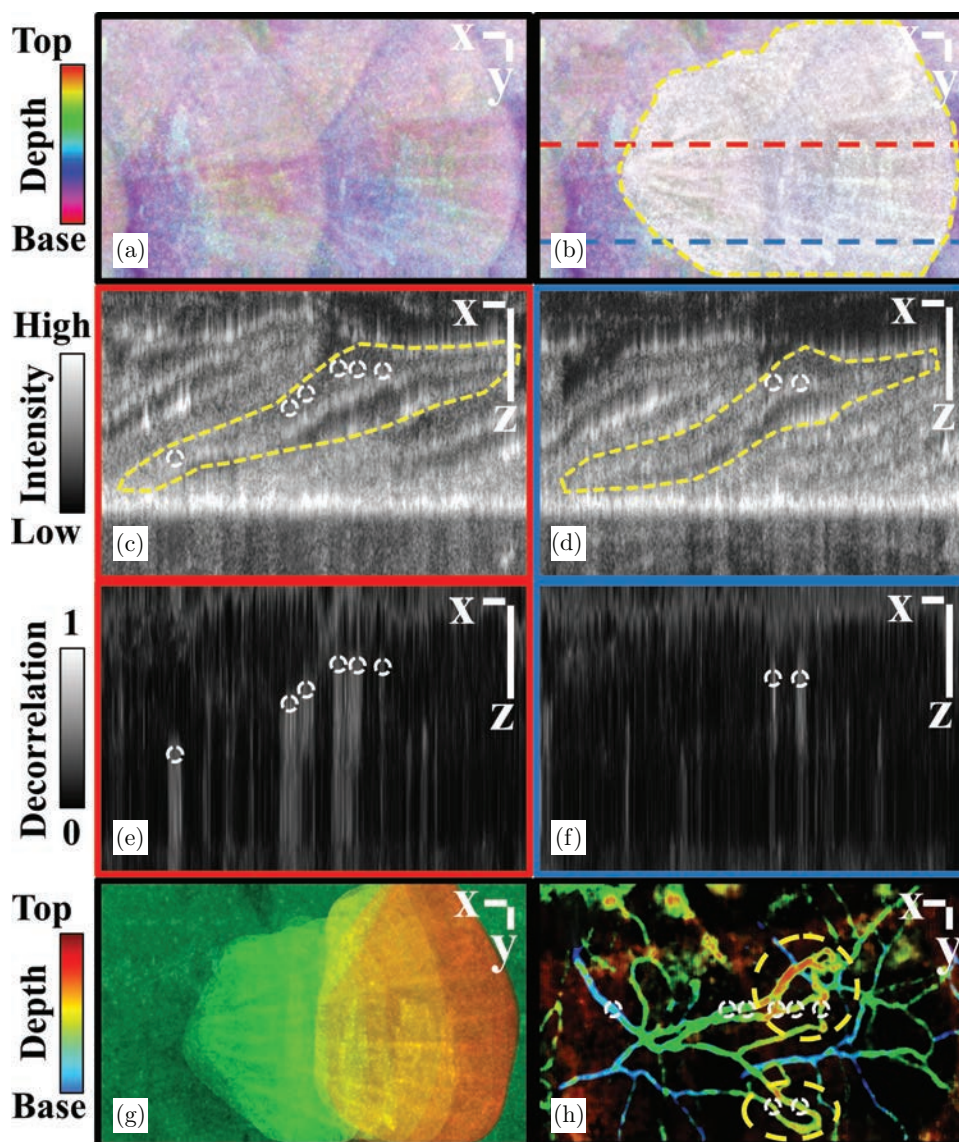Furthermore, we analyzed the spatial distribution of the skin vasculature, as shown in Fig. 6. A part of

Fig. 6. Spatial distribution of the skin vasculature. (a) is the depth-color encoded OCT intensity image of the scale area. (b) is generated by merging a single scale with OCT intensity information (marked by the yellow dashed curve) and the depth-color encoded OCT intensity image (a). (c) and (d) are B-scan OCT intensity images, corresponding to two positions of the middle area (marked by a red dashed line) and side area (marked by a blue dashed line) in (b), respectively. (e) and (f) are their B-scan OCTA images. (g) and (h) are the depth-color encoded OCT intensity and OCTA images, respectively. All scale bars are $100\,\mu m$.

the scale area of the 9-month-old zebrafish is shown in Fig. 6(a), which is a depth-color encoded OCT intensity image. We manually selected the single scale areas from each *en-face* intensity image at each depth and averaged intensities of selected areas as the intensity image of the single scale. And then, Fig. 6(a) and the intensity image of the single scale were merged, as shown in Fig. 6(b). The single scale area is marked by a yellow dashed curve in Fig. 6(b). As shown in Fig. 6(b), the radial grooves extend from the root of the scale to the outer end of the scale.

We randomly selected two positions at the middle area (marked by a red dashed line) and side area (marked by a blue dashed line) to analyze the axial distribution of the zebrafish skin, whose B-scan intensity images are shown in Figs. 6(c) and 6(d), respectively. The area of a single scale is manually selected by the yellow dashed curve. The scale is inserted into the zebrafish skin obliquely. A part of the scale is exposed and the other part is covered by other scales. The skin part shows high intensity, in contrast, the transparent bone matrix shows low intensity. The corresponding B-scan OCTA images are shown in Figs. 6(e) and 6(f). There are multiple blood vessels in the single-scale area (marked by small white dashed circles). The blood vessels in the middle area are distributed at different depths, and

those in the lateral area are distributed on the top of the scales. The blood vessels in the middle area are denser than those in the lateral area.

The depth-color encoded intensity and OCTA images are shown in Figs. 6(g) and 6(h) to describe the overall spatial distribution of a single scale. The scale, as well as the blood vessels, gradually extend into the skin from the top. The blood vessels in Figs. 6(e) and 6(f) are marked in Fig. 6(h). The blood vessels in the subcutaneous tissue extend, from left to right, to the surface of the scale. The two vascular bends marked by yellow dashed circles are the position of arteriovenous exchange.[6]

3.4. *Monitoring of zebrafish cutaneous wound healing*

Based on the above results, we performed imaging analysis on cutaneous wound healing. A total of 2–4 scales were removed from the zebrafish, and the injured location was imaged after different times. Figures 7(a)–7(c) and 7(d)–7(f) are corresponding to images at half an hour and 54.5 h, respectively. As shown in Fig. 7(a), a part of the scale missed, which shows low intensity (marked by a red dot-dashed closed curve). At 54.5 h, the skin has grown in the injured area (marked by a yellow dot-dashed closed curve in Fig. 7(d)). However, the bone matrix
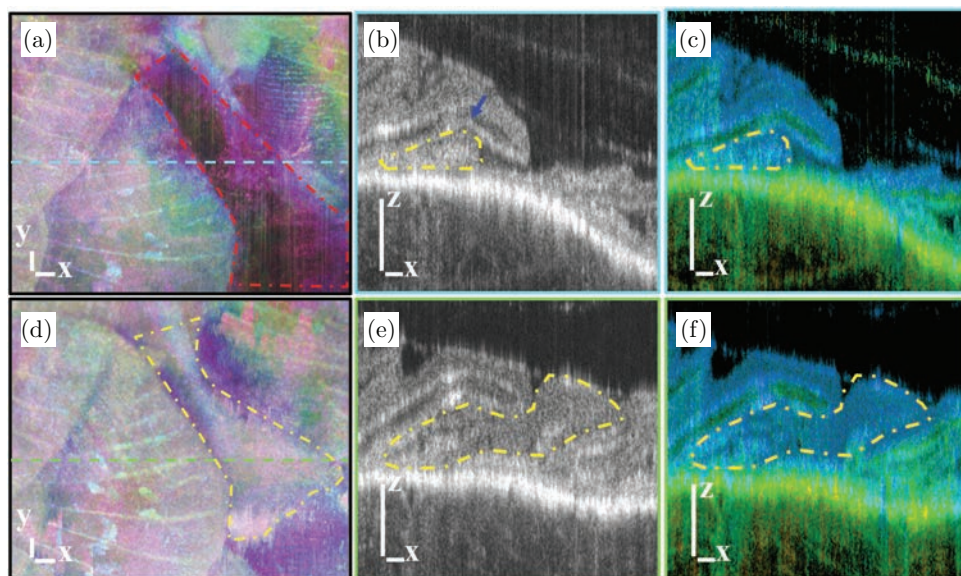

Fig. 7. Monitoring of zebrafish cutaneous wound healing with intensity and accumulative retardation images. (a)–(c) and (d)–(f) are images corresponding to half an hour and 54.5 h after the wound, respectively. (a) and (d) are the depth-color encoded OCT intensity images. (b) and (e) are B-scan OCT intensity images, (c) and (f) are B-scan OCT accumulative retardation images, which are corresponding to the positions marked by a blue dashed line and a green dashed line in (a) and (e), respectively. All scale bars are 100 μm.
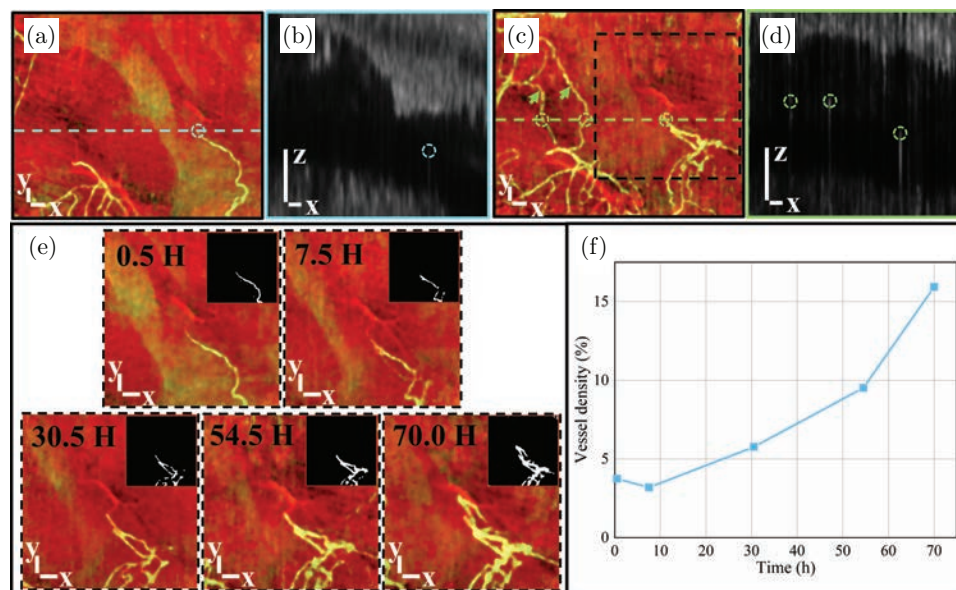
Fig. 8. Monitoring of zebrafish cutaneous wound healing with OCTA images. (a) and (c) are images merging the AIPs of OCTA within the skin area and the subcutaneous tissue area. (b) and (d) are B-scan OCTA images, which are corresponding to the positions marked by a blue dashed line and a green dashed line in (a) and (c), respectively. (e) is the monitoring results with time elapsing. Binary vessel maps based on a fixed threshold are shown in the upper right corner of each image in (e). (f) is the variation of vessel density during the monitoring process. All scale bars are 100 μm.

has not formed. Thus, the radial grooves cannot be observed. We selected similar positions of the zebrafish skin at different times to analyze the axial information of the zebrafish skin, marked by a blue dashed line and a green dashed line in Figs. 7(a) and 7(d), respectively. The corresponding B-scan OCT intensity images are shown in Figs. 7(b) and 7(c), and accumulative retardation images are shown in Figs. 7(e) and 7(f). In Figs. 7(b) and 7(c), the scale was peeled off and only a little part of the scale remained (marked by a yellow dot-dashed closed curve). Due to skin damage and loss of support, the adjacent scale on the left had a fracture covering the root of the remaining scale (pointed out by a blue arrow). At 54.5 h, as shown in Figs. 7(e) and 7(f), the new skin tissue (marked by a yellow dot-dashed closed curve) filled the missing area. However, the bone formation has not been observed in the injured area. The retardation of the injured area was still kept low during this recovery process.

Furthermore, we analyzed the OCTA images with images merging the AIPs of OCTA within the skin area and the subcutaneous tissue area [Figs. 8(a) and 8(c)]. The B-scan OCTA images [Figs. 8(b) and 8(d)] are the corresponding areas marked by a blue dashed line in Fig. 8(a) and a green dashed line in Fig. 8(c). The blood vessels

were missing in the injured area at half an hour. Although the adjacent scale on the right was injured, a single blood vessel (marked by a small blue dashed circle in Fig. 8(b)) close to the base of the skin is observed. At 54.5 h, the blood vessels in the residual area were reconstructed, and the blood vessels of the adjacent scale on the right side remained in place (marked by several small green dashed circles in Fig. 8(d)).

Based on images merging the AIPs of OCTA within the skin area and the subcutaneous tissue area [Figs. 8(a) and 8(c)], the process of vessel reconstruction can be observed more clearly. The blood vessels in this area are damaged due to the loss of the scales, resulting in the destruction of the skin attached to the scales. At half an hour, damaged blood vessels are still not recovered, so the absence of blood vessels is shown in Fig. 8(a) and only a blood vessel (marked by a small blue dashed circle) can be observed on the right side. The single blood vessel is connected with the blood vessel of the subcutaneous tissue. At 54.5 h, blood vessels in the residual part of the injured area are reconstructed (pointed out by green arrows in Fig. 8(c)), and new blood vessels are formed. The small dashed circles in Figs. 8(a) and 8(b), and 8(c) and 8(d) correspond to the same blood vessels, respectively.

To observe the changes of blood vessels with time elapsing, we monitored the pressure-damaged area (marked by a black dashed box in Fig. 8(c)) and the monitoring results at different times are shown in Fig. 8(e). The new blood vessels gradually extend from the junction of subcutaneous blood vessels, and gradually form multiple branches. For quantitative analysis of vessels, we generated binary vessel maps of Fig. 8(e) based on a fixed threshold shown in the upper right corner of each image in Fig. 8(e), and the vessel density (VD) was calculated from those binary vessel maps. As shown in Fig. 8(f), we can observe gradually increasing VD during the recovery process of the skin, which indicates the reconstruction of blood vessels in zebrafish in line with the characteristics of the proliferation stage.[3]

4. Discussion

PS-OCT and OCTA images of zebrafish skin were obtained by our homemade high-resolution PS-OCT system, which were used to analyze the spatial distribution of zebrafish skin vasculatures, and the short-term healing process of the cutaneous wound was monitored. The combination of PS-OCT and OCTA demonstrated their ability to image the skin internal structure and blood vessels of the zebrafish skin while assessing its recovery.

Compared with OCT system with the center wavelength of 1300 nm or 1060 nm, 840 nm SD-OCT system can obtain a higher spatial resolution. High-resolution PS-OCT and OCTA images can provide more details for the spatial distribution and polarimetric properties of zebrafish skin. In this paper, by the high-resolution PS-OCT system, the thin radial grooves were shown with high birefringence, and the OCTA images display the micronscale vasculature distributed in different depths of the skin. During the healing process of zebrafish skin injury, subtle changes in blood vessels and skin structure were revealed by our PS-OCT system.

Polarization images have different sensitivities to different pigments. The stripe of yellow xanthophores shows high accumulative retardation due to its depolarization. The intensity image cannot easily describe the composition of the tissue, and the intensity of the zebrafish is more likely to be affected in the liquid environment. Zebrafish stripe is the model for vertebrate color pattern formation.[31] Inflammation drives wound hyperpigmentation in zebrafish by recruiting pigment cells to sites of tissue damage.[32] As known in our results, accumulative retardation, as one of the polarization characteristics of PS-OCT, is sensitive to the pigmentation of tissue. Therefore, retardation has an important auxiliary value in the pigmentation study of zebrafish skin.

We described the zebrafish skin vasculature and gave representative results based on the OCTA method in this paper. As described in Ref. 6, the distribution of blood vessels in the zebrafish is regular. We imaged the skin vessels of zebrafish at different ages (2 months old and 9 months old). Compared with the result in Ref. 6, similar blood vessel distributions were shown to prove the correctness of the OCTA method in zebrafish vascular imaging.

The fluorescence microscopy imaging method is usually used for imaging the zebrafish skin vessels but has limited imaging penetration depth and needs a complex operation to require specific fluorescent labeling. Compared with fluorescence microscopy imaging,[6] we demonstrated the ability of OCTA technology to image the blood vessels in the zebrafish subcutaneous tissue, showing the connection relationship between the blood vessels in the skin. After that, we described the spatial distribution information of the blood vessels on a single scale.

For *in vivo* zebrafish imaging, one of the shortcomings for OCTA is that fluid may induce imaging artifacts because the zebrafish is in the liquid environment. The other shortcoming is the motion artifact from the zebrafish. Therefore, when designing an anesthesia imaging system, it is necessary to ensure that the zebrafish skin is above the level of the anesthesia liquid. On the other hand, deep anesthesia is required for the zebrafish to remain stationary. The anesthetic dose and circulatory system used in this experiment ensured that the zebrafish was under anesthesia for a long time (longer than 10 h), providing the possibility for multiple imaging in a long period. It should be noted that the system must be at a suitable room temperature (24–30°C), and a heating device can be added to maintain the temperature.

Due to the long monitoring interval, zebrafish need to wake up after each measurement and be anaesthetized again before the next measurement. Therefore, its position cannot be the same at each time, and the zebrafish injury size is very small. During the measurement, we placed the wound position as far as possible in the scanning field of

view through observation. During image processing, we manually cropped the area of interest based on a marker point in the image. In future studies requiring long-term monitoring of zebrafish, fixed-range images can be obtained by optimizing zebrafish fixtures and positioning systems.

Based on this study, it is proven that it is possible to study the state of subcutaneous tissue during cutaneous wound healing. With the suitable imaging depth and the role of the polarization parameters in the quantitative analysis of zebrafish muscles,[26] our PS-OCT system can comprehensively monitor and describe the healing process of zebrafish for a long period.

SSADA algorithm, as one of the intensity-signal-based OCTA methods, uses the segmented spectral information to improve the DSNR. This kind of spectral calculation idea is also suitable for suppressing noise for calculating polarization information. Thus, it is feasible to be incorporated into the PS-OCT algorithm. However, the resolution in the axial direction is reduced with the low bandwidth of filters. In this study, we found the Gaussian filtering of SSADA is the same as the method of down-sampling in our previous axial super-resolution study,[33,34] which means the combination of the segmented spectral information and deep learning methods will improve the resolutions of PS-OCT and OCTA images, and we will further study them in detail.

In this study, we monitored the wound healing process of zebrafish skin. The vessel density of the zebrafish skin showed an increasing trend within 70 h. Our result is consistent with the research result on the wound healing process of human skin, which showed an increase in blood vessel density within five days of injury.[35] Both results are in line with the characteristics of the proliferation stage.[3] In future studies, we will compare the complete vascular recovery cycle of zebrafish with that of the human in detail.

5. Conclusion

We demonstrated the ability of our PS-OCT system for imaging the skin internal structure and zebrafish skin vasculature in this paper. We clearly observed the polarization and flow characteristics of zebrafish skins at different ages (2 months and 9 months old) with our PS-OCT system. Based on the intensity and OCTA images, we described the spatial distribution of the zebrafish skin vasculature. Moreover, we monitored the process of zebrafish cutaneous wound healing by our system. We have demonstrated the utility of PS-OCT and OCTA for structural and functional imaging of the zebrafish skin. We believe the high-resolution PS-OCT system has great potential in zebrafish cutaneous research.

Conflicts of Interest

The authors declare that there are no conflicts of interest relevant to this paper.

Acknowledgments

References

1. G. Broughton 2nd, J. E. Janis, C. E. Attinger, "The basic science of wound healing," *Plast. Reconstr. Surg.* **117**(7S), 12S–34S (2006).

2. G. C. Gurtner, S. Werner, Y. Barrandon, M. T. Longaker, "Wound repair and regeneration," *Nature* **453**(7193), 314–321 (2008).

3. K. E. Johnson, T. A. Wilgus, "Vascular endothelial growth factor and angiogenesis in the regulation of cutaneous wound repair," *Adv. Wound Care* **3**(10), 647–661 (2014).

4. R. Richardson, K. Slanchev, C. Kraus, P. Knyphausen, S. Eming, M. Hammerschmidt, "Adult zebrafish as a model system for cutaneous wound-healing research," *J. Invest. Dermatol.* **133**(6), 1655–1665 (2013).

5. F. Bootorabi, H. Manouchehri, R. Changizi, H. Barker, E. Palazzo, A. Saltari, M. Parikka, C. Pincelli, A. Aspatwar, "Zebrafish as a model organism for the development of drugs for skin cancer," *Int. J. Mol. Sci.* **18**(7), 1550 (2017).

6. C. Noishiki, S. Yuge, K. Ando, Y. Wakayama, N. Mochizuki, R. Ogawa, S. Fukuhara, "Live imaging of angiogenesis during cutaneous wound healing in adult zebrafish," *Angiogenesis* **22**(2), 341–354 (2019).

7. R. Richardson, M. Metzger, P. Knyphausen, T. Ramezani, K. Slanchev, C. Kraus, E. Schmelzer,

M. Hammerschmidt, "Re-epithelialization of cutaneous wounds in adult zebrafish combines mechanisms of wound closure in embryonic and adult mammals," *Development* **143**(12), 2077–2088 (2016).

8. M. Iwasaki, J. Kuroda, K. Kawakami, H. Wada, "Epidermal regulation of bone morphogenesis through the development and regeneration of osteoblasts in the zebrafish scale," *Dev. Biol.* **437**(4), 105–119 (2018).

9. D. E. Dalle Nogare, N. Natesh, H. D. Vishwasrao, H. Shroff, A. B. Chitnis, "Zebrafish posterior lateral line primordium migration requires interactions between a superficial sheath of motile cells and the skin," *Elife* **9**, e58251 (2020).

10. J. Delcourt, M. Ovidio, M. Denoël, M. Muller, H. Pendeville, J.-L. Deneubourg, P. Poncin, "Individual identification and marking techniques for zebrafish," *Rev. Fish Biol. Fisher.* **28**(4), 839–864 (2018).

11. H. Li, K. Liu, L. Yao, X. Deng, Z. Zhang, P. Li, "ID-OCTA: OCT angiography based on inverse SNR and decorrelation features," *J. Innov. Opt. Health Sci.* **14**(01), 2130001 (2021).

12. C.-L. Chen, R. K. Wang, "Optical coherence tomography based angiography [Invited]," *Biomed. Opt. Express* **8**(2), 1056–1082 (2017).

13. J. Liu, J. Fan, Q. Wang, W. He, C. Dong, M. Sun, G. Shi, "Observation of the early blood vessels of cutaneous malignant melanoma using swept source optical coherence tomography angiography (SS-OCTA)," *J. Innov. Opt. Health Sci.* **12**(04), 1942005 (2019).

14. Z. Zhang, T. Zhu, T. Cao, Z. Gong, L. Yao, K. Liu, J. Ye, P. Li, "Swept source intraoperative OCT angiography," *J. Innov. Opt. Health Sci.* **14**(01), 2140009 (2021).

15. O. Nadiarnykh, V. Davidoiu, M. G. O. Gräfe, M. Bosscha, A. C. Moll, J. F. de Boer, "Phase-based OCT angiography in diagnostic imaging of pediatric retinoblastoma patients: abnormal blood vessels in post-treatment regression patterns," *Biomed. Opt. Express* **10**(5), 2213–2226 (2019).

16. Z. Hu, Y. Su, P. Xie, L. Chen, J. Ji, T. Feng, S. Wu, K. Liang, Q. Liu, "OCT angiography-based monitoring of neovascular regression on fibrovascular membrane after preoperative intravitreal conbercept injection," *Graefe's Arch. Clin. Exp. Ophthalmol.* **257**(8), 1611–1619 (2019).

17. Z. Chu, C.-L. Chen, Q. Zhang, K. Pepple, M. Durbin, G. Gregori, R. K. Wang, "Complex signal-based optical coherence tomography angiography enables in vivo visualization of choriocapillaris in human choroid," *J. Biomed. Opt.* **22**(12), 121705 (2017).

18. P. Gong, Q. Li, Q. Wang, K. Karnowski, D. D. Sampson, "Jones matrix-based speckle-decorrelation angiography using polarization-sensitive optical coherence tomography," *J. Biophotonics* **13**(9), e202000007 (2020).

19. P. Tang, R. K. Wang, "Polarization sensitive optical coherence tomography for imaging microvascular information within living tissue without polarization-induced artifacts," *Biomed. Opt. Express* **11**(11), 6379–6388 (2020).

20. K. S. Park, W. J. Choi, S. Song, J. Xu, R. K. Wang, "Multifunctional in vivo imaging for monitoring wound healing using swept-source polarization-sensitive optical coherence tomography," *Lasers Surg. Med.* **50**(3), 213–221 (2018).

21. E. Li, S. Makita, Y.-J. Hong, D. Kasaragod, Y. Yasuno, "Three-dimensional multi-contrast imaging of *in vivo* human skin by Jones matrix optical coherence tomography," *Biomed. Opt. Express* **8**(3), 1290–1305 (2017).

22. Y. Lin, X. Xiang, T. Chen, C. Gao, H. Fu, L. Wang, L. Deng, L. Zeng, J. Zhang, "*In vivo* monitoring and high-resolution characterizing of the prednisolone-induced osteoporotic process on adult zebrafish by optical coherence tomography," *Biomed. Opt. Express* **10**(3), 1184–1195 (2019).

23. Y. Lin, T. Chen, G. Mao, T. Qiu, Y. Lan, X. Xiang, J. Huang, J. Huang, T. Lu, S. Gan, X.-D. Sun, J. Zhang, "Long-term and in vivo assessment of Aβ protein-induced brain atrophy in a zebrafish model by optical coherence tomography," *J. Biophotonics* **13**(7), e202000067 (2020).

24. I. Bozic, X. Li, Y. Tao, "Quantitative biometry of zebrafish retinal vasculature using optical coherence tomographic angiography," *Biomed. Opt. Express* **9**(3), 1244–1255 (2018).

25. Y. Chen, L. A. Trinh, J. Fingler, S. E. Fraser, "Phase variance optical coherence microscopy for label-free imaging of the developing vasculature in zebrafish embryos," *J. Biomed. Opt.* **21**(12), 126022 (2016).

26. D. Yang, M. Hu, M. Zhang, Y. Liang, "High-resolution polarization-sensitive optical coherence tomography for zebrafish muscle imaging," *Biomed. Opt. Express* **11**(10), 5618–5632 (2020).

27. Y. Jia, O. Tan, J. Tokayer, B. Potsaid, Y. Wang, J. J. Liu, M. F. Kraus, H. Subhash, J. G. Fujimoto, J. Hornegger, D. Huang, "Split-spectrum amplitude-decorrelation angiography with optical coherence tomography," *Opt. Express* **20**(4), 4710–4725 (2012).

28. S. S. Gao, G. Liu, D. Huang, Y. Jia, "Optimization of the split-spectrum amplitude-decorrelation angiography algorithm on a spectral optical coherence tomography system," *Opt. Lett.* **40**(10), 2305–2308 (2015).

29. V. J. Srinivasan, E. T. Mandeville, A. Can, F. Blasi, M. Climov, A. Daneshmand, J. H. Lee, E. Yu, H. Radhakrishnan, E. H. Lo, S. Sakadžić, K. Eikermann-Haerter, C. Ayata, "Multiparametric, longitudinal optical coherence tomography imaging reveals acute injury and chronic recovery in experimental ischemic stroke," *PLoS One* **8**(8), e71478 (2013).

30. C. Magnain, J. C. Augustinack, M. Reuter, C. Wachinger, M. P. Frosch, T. Ragan, T. Akkin, V. J. Wedeen, D. A. Boas, B. Fischl, "Blockface histology with optical coherence tomography: A comparison with Nissl staining," *NeuroImage* **84**, 524–533 (2014).

31. A. P. Singh, C. Nüsslein-Volhard, "Zebrafish stripes as a model for vertebrate colour pattern formation," *Curr. Biol.* **25**(2), R81–R92 (2015).

32. M. Lévesque, Y. Feng, R. A. Jones, P. Martin, "Inflammation drives wound hyperpigmentation in zebrafish by recruiting pigment cells to sites of tissue damage," *Dis. Model. Mech.* **6**(2), 508–515 (2013).

33. Z. Yuan, D. Yang, H. Pan, Y. Liang, "Axial super-resolution study for optical coherence tomography images via deep learning," *IEEE Access* **8**, 204941–204950 (2020).

34. H. Pan, D. Yang, Z. Yuan, Y. Liang, "More realistic low-resolution OCT image generation approach for training deep neural networks," *OSA Contin.* **3**(11), 3197–3205 (2020).

35. P. Gong, S. Es'haghian, F. M. Wood, D. D. Sampson, R. A. McLaughlin, "Optical coherence tomography angiography for longitudinal monitoring of vascular changes in human cutaneous burns," *Exp. Dermatol.* **25**(9), 722–724 (2016).